



Research Paper

Scalable one-step production of porous oxygen-doped g-C₃N₄ nanorods with effective electron separation for excellent visible-light photocatalytic activity

Yunxiong Zeng^{a,1}, Xia Liu^{b,1}, Chengbin Liu^{a,*}, Longlu Wang^a, Yingchun Xia^a, Shuqu Zhang^a, Shenglian Luo^a, Yong Pei^b

^a State Key Laboratory of Chemo/Biosensing and Chemometrics, Hunan University, Changsha 410082, PR China

^b Department of Chemistry, Xiangtan University, Xiangtan 411105, China

ARTICLE INFO

Keywords:

Scalable bottom-up production
Oxygen-doped g-C₃N₄ nanorod
Electron/hole separation
Photocatalytic H₂ evolution
Photocatalytic degradation

ABSTRACT

Photoinduced electron transfer and separation from its home atom to form spatial isolated electron/hole pairs is the most crucial factor in artificial photocatalysis field. The scalable production of nanoscale g-C₃N₄ with remarkable electron separation efficiency in one-step, green, economic and “bottom-up” approach is of great challenge. Herein, one-dimensional porous architectural g-C₃N₄ nanorods have been facilely prepared by direct calcination of hydrous melamine nanofibers precipitated from aqueous solution of melamine. Porous morphologies with increased interfacial area enhance light capture capacity and accelerate catalysis reaction. It is noted that oxygen atoms were simultaneously doped into g-C₃N₄ matrix, which broke the symmetry of pristine g-C₃N₄, resulting in more effective separation of electron/hole pairs. Thus, the oxygen-doped g-C₃N₄ nanorods loaded with Pt presented excellent visible-light photocatalytic hydrogen evolution in the triethanolamine solution (732 μmol g⁻¹ h⁻¹) and in overall water splitting (29.6 μmol g⁻¹ h⁻¹), and 2,4-dinitrophenol degradation for O-doped g-C₃N₄ nanorod (removal efficiency of 100% within 75 min). Subsequently, the visible-light photocatalytic H₂ evolution (96 μmol g⁻¹ h⁻¹) with simultaneous 2,4-dinitrophenol degradation were achieved for Pt@g-C₃N₄ nanorod. The proposed synthesis strategy overcomes long-standing, stubborn and serious stacking/agglomeration for g-C₃N₄ synthesis, and paves the pathway for industrial scale-up production of high-performance g-C₃N₄ and application in practical energy and environment area.

1. Introduction

Graphite-like carbon nitride (g-C₃N₄) has attracted wide-spread attention in artificial photosynthesis and solar energy conversion/storage due to its desirable visible-light response, environment-friendly and low-cost merits as well as adjustable electronic properties [1–3]. However, the photocatalytic efficiency of pristine g-C₃N₄ is severely limited by poor light harvesting, fast photoinduced hole/electron pair recombination and sluggish H₂-evolving reaction [3–5]. In generally, nano-structural engineering is considered as one of the most ideal strategies to enhance light absorption capacity and accelerate photocatalytic reaction [6,7]. The more important thing is to extract photo-generated electron off its home atom to form spatially isolated electron/hole pairs as possible as we can [8–11]. Thus, doping with heteroatoms and molecules, coupling with semiconductors and manufacturing specified defect approaches have been widely developed to cope with

unsatisfied charge utilization efficiency [12–14]. Heterostructure construction with other semiconductors is extensively employed to suppress photo-excited electron/hole recombination, nevertheless, photo-redox potential of composite towards substrates is inevitably weakened to some extent [15,16]. Heteroatom and molecule doped into g-C₃N₄ modulating electron and bandgap structure have been demonstrated to effectively improve catalytic activity [17–19]. Merely taking sole measurement to tune g-C₃N₄ electron/hole transfer, separation and catalytic performance is far from enough in artificial photosynthesis energy conversion [20,21].

Photogenerated electron separation and transfer modulation with simultaneous nanostructure and morphology tunableness towards pristine g-C₃N₄ are extremely mainstream and acceptable [22–24]. Hitherto, researches about scalable production of nanoscale g-C₃N₄ with superior excited electron utilization efficiency in a green, economic and bottom-up approach are rarely reported [25–27]. For this purpose, we

* Corresponding author.

E-mail address: chem_cblu@hnu.edu.cn (C. Liu).

¹ These authors contributed equally to this work.

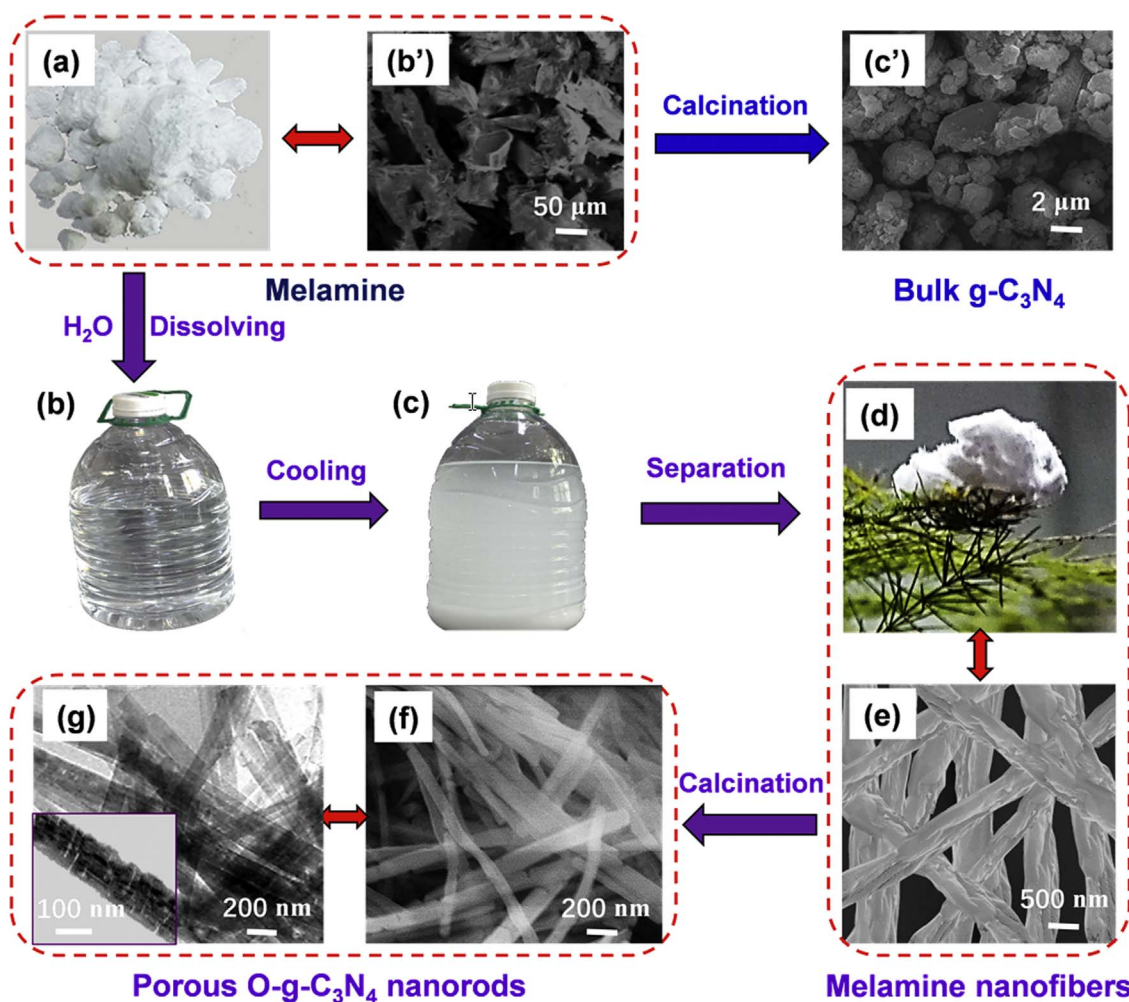
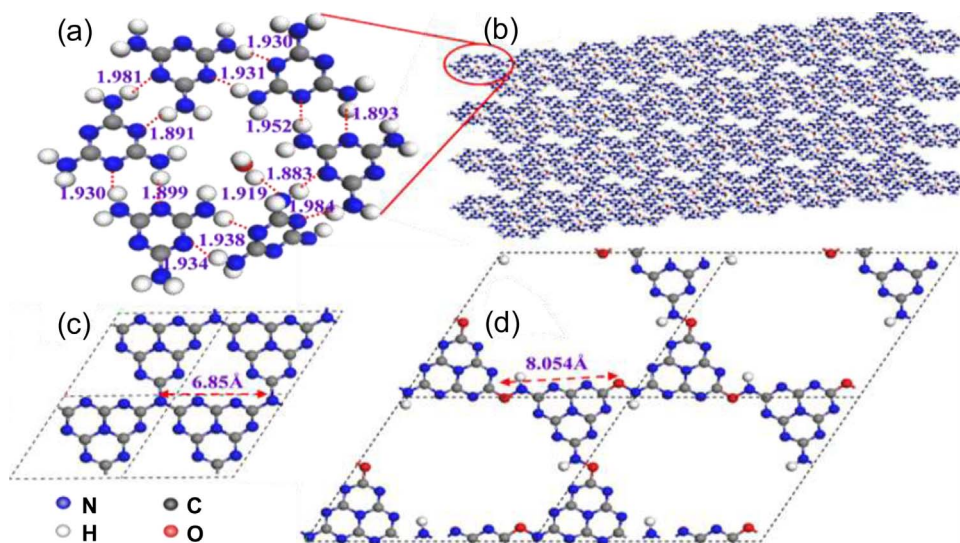


Fig. 1. (a–g) Synthesis procedure of porous O-g-C₃N₄ NR and (a, b', and c') direct calcination synthesis of bulk g-C₃N₄: photographs of (a) melamine powder, (b) melamine aqueous solution, (c) melamine precipitation and (d) collected melamine precipitate, (e) SEM image of hydrous melamine nanofibers, (f) SEM image of O-g-C₃N₄ NR, (g) TEM image of O-g-C₃N₄ NR (inset is the magnified TEM image), (b') SEM image of melamine, and (c') SEM image of bulk g-C₃N₄ from direct calcination of melamine powder.



Scheme 1. Optimized structures: (a and b) self-assembly of melamine, (c) pristine g-C₃N₄ and (d) O-g-C₃N₄.

designed and prepared one-dimensional (1D) oxygen doped g-C₃N₄ nanorods (O-g-C₃N₄ NR) by direct calcination of hydrous melamine nanofibers precipitated from aqueous solution of melamine (Fig. 1). Bulky melamine powder was dissolved in distilled water with vigorous stirring, and the numerous hydrophilic –NH₂ groups in tri-s-triazine

ring interacted with H₂O to form hydrogen-bonding complexes [28,29]. As temperature gradually dropping down, the melamine complexes gradually precipitated from water accompanying the formation of nanofibers by self-assembly in which the inserted H₂O molecules were locked in the cage made of surrounded melamine molecules (Scheme

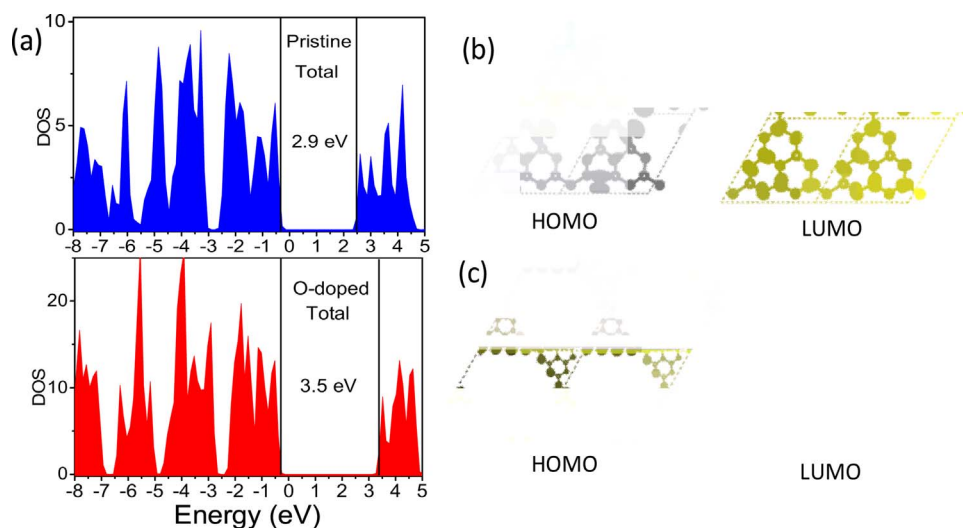


Fig. 2. (a) Density of state (DOS) of pristine $g\text{-C}_3\text{N}_4$ (up) and $\text{O-g-C}_3\text{N}_4$ NR (down) from HSE06 calculations, (b) Kohn-Sham orbitals for the valence and conduction band of pristine $g\text{-C}_3\text{N}_4$, and (c) Kohn-Sham orbitals for the valence and conduction band of $\text{O-g-C}_3\text{N}_4$ NR. The carbon, nitrogen and oxygen atoms are grey, blue and red respectively. The isodensity surfaces are drawn for a charge density of $0.01\text{qe}\text{\AA}^{-3}$. (For interpretation of the references to color in this figure legend, the reader is referred to the web version of this article.)

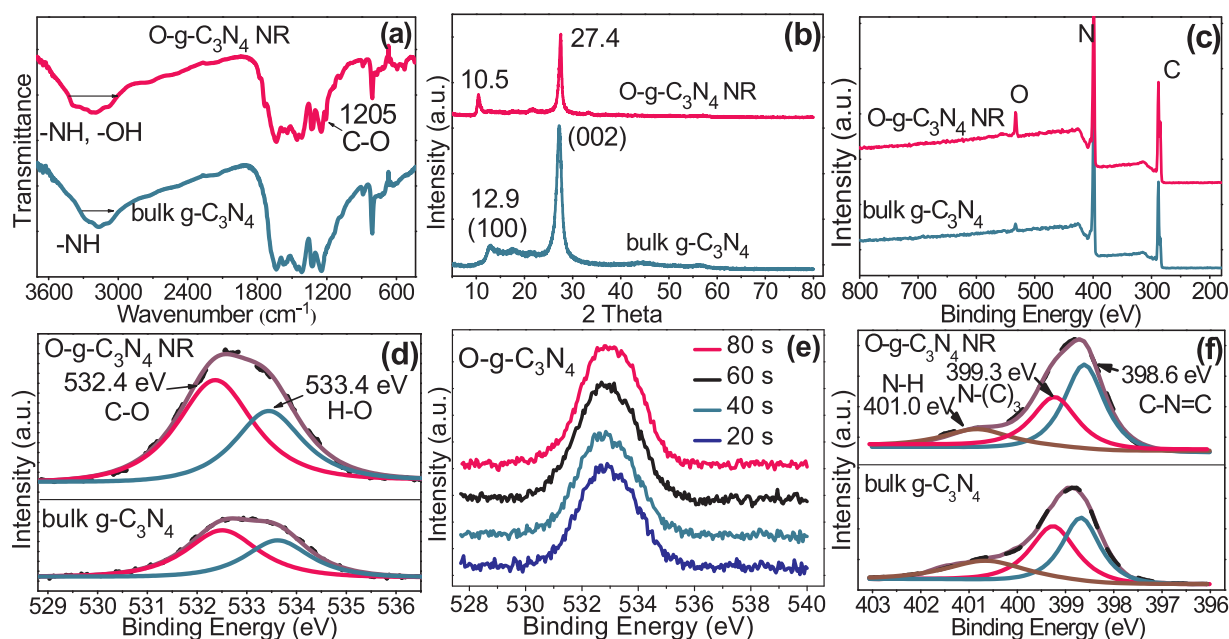
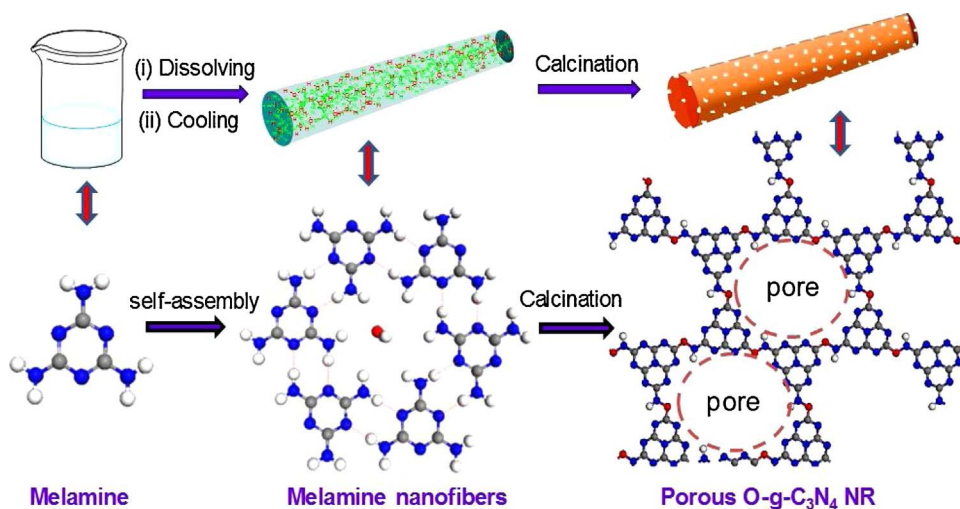


Fig. 3. (a) FT-IR spectra, (b) XRD patterns and (c) full XPS spectra of bulk $g\text{-C}_3\text{N}_4$ and $\text{O-g-C}_3\text{N}_4$ NR; (d) high-resolution XPS spectra and (e) high-resolution XPS spectra upon Ar^+ sputtering of O; (f) high-resolution XPS spectra of N 1s.



Scheme 2. Schematic illustration of $\text{O-g-C}_3\text{N}_4$ NR formation: morphologies (top) and structures (bottom).

1). Finally, the hydrous melamine nanofibers were polymerized into 1D g-C₃N₄ nanorods by calcination. The g-C₃N₄ nanorod was not only featured by porous morphology, enhancing light absorption, increasing interfacial area and accelerating surface reaction, but also doped by oxygen atoms, pushing photogenerated electron off its home atom to form spatially separated electron/hole pairs. To sum up, this is a “two-in-one” strategy by which nanoengineering and doping are achieved simultaneously. The oxygen doped porous g-C₃N₄ nanorods exhibited outstanding visible-light photocatalytic activities towards overall water splitting and intractable organic pollutant degradation with simultaneous H₂ production.

2. Experimental section

2.1. Chemicals

All the reagents were purchased from Sinopharm Chemical Reagent Co. Ltd and used without further purification. Distilled water was used in the whole experiment process.

2.2. Synthesis of O-g-C₃N₄ NR and bulk g-C₃N₄

At first, commercial melamine powder (60 g, 476.2 mmol) was dissolved in distilled water (13.0 L) at 40 °C under stirring until complete dissolution. Afterwards, the melamine solution was filtered to remove solid residue. The filtrate was further gradually cooled down below room temperature (approximately 4 °C) in a refrigerator to get a white flocculent solid. The collected solid (45 g, 357.2 mmol) was dried at 60 °C in a vacuum oven to get rid of unbound water. Finally, the dried solid (5 g) was calcined in a luminum crucible sealed with a lid from room temperature to 500 °C at a heating rate of 1 °C/min under N₂ atmosphere for 2 h, and then cooled to room temperature to obtain oxygen-doped g-C₃N₄ nanorods (O-g-C₃N₄ NR) (1.5 g). As a control, bulk g-C₃N₄ was prepared by directly heating commercial melamine powder (5 g, 39.7 mmol) in a tube furnace from room temperature to 500 °C at a heating rate of 1 °C/min under N₂ atmosphere for 2 h, followed by cooling to room temperature naturally.

2.3. Characterization

The morphologies and composition of samples were characterized by powder X-ray diffraction (XRD) with Cu-K α radiation (Rigaku, Smartlab), UV–vis diffuse reflectance spectrophotometer (DRS) (Agilent, Cary 300), nuclear magnetic resonance (NMR) spectra (Bruker, 400MHz) with tetramethylsilane (TMS) as an internal standard and DMSO as solvent, thermogravimetric analysis (TG) (TG/DTA7300, Germany), the Fourier transform infrared (FT-IR) spectra (Thermo Fisher Scientific), transmittance electron microscopy (TEM) (JEOL, JEM-2100F), field emission scanning electron microscopy (FE-SEM) with energy dispersive X-ray (EDX) (Hitachi, S-4800), and high-resolution X-ray photoelectron spectroscopy (XPS) with Al-K α radiation and Ar⁺ sputtering model (K-Alpha 1063, Thermo Fisher Scientific, England). The specific surface areas were determined by the Brunauer-Emmett-Teller (BET) method with N₂ adsorption at 77 K (Bel Japan Inc., BELSORP-mini II). The photoluminescence (PL) spectra were recorded with Hitachi F-7000 fluorescence spectrophotometer. The chemical element compositions were analyzed by EDS mapping images captured on a Tecnai G2 F20 S-TWIN atomic resolution analytical microscope. The time-resolved transient photoluminescence (TRPL) spectrum was performed using Hamamatsu universal streak camera C10910. Electron spin resonance (ESR) measurement was performed on a JES FA200(JEOL) spectrometer at room temperature. The as-prepared samples were loaded in a quartz tube and microwave frequency was maintained in the range from 9.00 to 9.70 GHz (X-band), and the microwave power was fixed at ~1.0 mW to avoid saturation.

2.4. Photoelectrochemical measurement

The photocurrents and Nyquist plot without bias potential were carried out with a CHI 660C electrochemical analyzer (CHI Inc., USA) in 0.5 M Na₂SO₄ aqueous solution with a three-electrode configuration: FTO electrodes deposited with the samples as the photoanode, a platinum wire as the counter electrode, and a saturated calomel electrode (SCE) as the reference electrode. All the samples were analyzed under room temperature. For the fabrication of the photoanode, 0.25 g of the sample was grinded with 0.06 g polyethylene glycol (PEG) and 0.5 mL ethanol to make a slurry. Then, the slurry was coated onto a 1 cm \times 4 cm FTO electrode by the doctor blade technique, and then allowed to dry in air. A 300 W xenon arc lamp with lighting wavelength range of 320–780 nm (Perfect-light, PLS-SXE 300C, Beijing) was used as light source.

2.5. Photocatalytic activity evaluation

Firstly, Pt particles as cocatalyst were photodeposited on O-g-C₃N₄ NR or bulk g-C₃N₄ in 15 vol% triethanolamine (TEOA) and H₂PtCl₆ solution using a full arc light ($\lambda > 300$ nm) for 2 h irradiation. The Pt content was adjusted with H₂PtCl₆ concentration and determined by inductively coupled plasma (ICP, PE5300DV). The photocatalytic H₂ evolution experiments were performed in a 100 mL sealed quartz flask at 5 °C. A 300 W xenon arc lamp with a 420 nm wavelength cutoff filter (Perfect light, PLS-SXE 300C, Beijing, China) was used as a visible light source to trigger the photocatalytic reaction. The Xe lamp was positioned 20 cm away from the reactor where the focused intensity on the flask was 120 mW cm⁻². In a photocatalytic experiment, photocatalyst sample (25 mg) was dispersed in a solution containing TEOA as sacrificial agents (15 vol%, 80 mL) for H₂ production, distilled water only (80 mL) for overall water splitting, or 2,4-dinitrophenol (2,4-DNP) (80 mL, 10 mg L⁻¹) for simultaneous H₂ evolution with 2,4-DNP degradation, respectively. Before irradiation, these systems were bubbled with nitrogen for 30 min to remove the air ensuring the reaction system in an inertial condition. The H₂ was analyzed by a gas chromatography with 5 Å molecular sieve column (Shimadzu, GC2010). For only photocatalytic degradation of 2,4-DNP, the experiment conditions were the same as above but without bubbling nitrogen. The real-time concentration of 2,4-DNP was determined by its characteristic maximum peak using a UV–vis spectrophotometer (Varian, Cary 300). The total organic carbon (TOC) was measured using a TOC analyzer (TOC-VCPh/CPN, Shimadzu).

3. Results and discussion

3.1. Morphology and structure characterization

The synthesis procedure was demonstrated in Fig. 1. The melamine powder was dissolved in hot water, interacting with H₂O molecules by hydrogen-bond (Fig. 1a and b), and then gradually precipitated along with temperature slightly cooling down (Fig. 1c). The collected melamine precipitate featured cotton-like appearance on the leaf tip (Fig. 1d). Interestingly, the melamine precipitate consisted of nanofibers with a diameter of ca. 600 nm (Fig. 1e). ¹H NMR characterization was carried out to confirm the occurrence state of H₂O molecules in melamine nanofibers. As shown in Fig. S1a, the peak at 3.34 ppm appeared in melamine fibers, which was contributed to H₂O molecules locked in the melamine hydrate fibers. In sharp contrast, the peak intensity at 3.34 ppm was pretty puny for commercial melamine. Nevertheless, peak intensity is positively related with element content in sample, and the frail intensity at 3.34 pm in bare melamine indicates trace amount of H₂O, ascribed to H₂O absorbed on the surface of melamine. In addition, TG results showed that the decomposition of melamine occurred at 215 °C for bare melamine, while the initial weight loss of melamine nanofibers occurred at 170 °C due to the

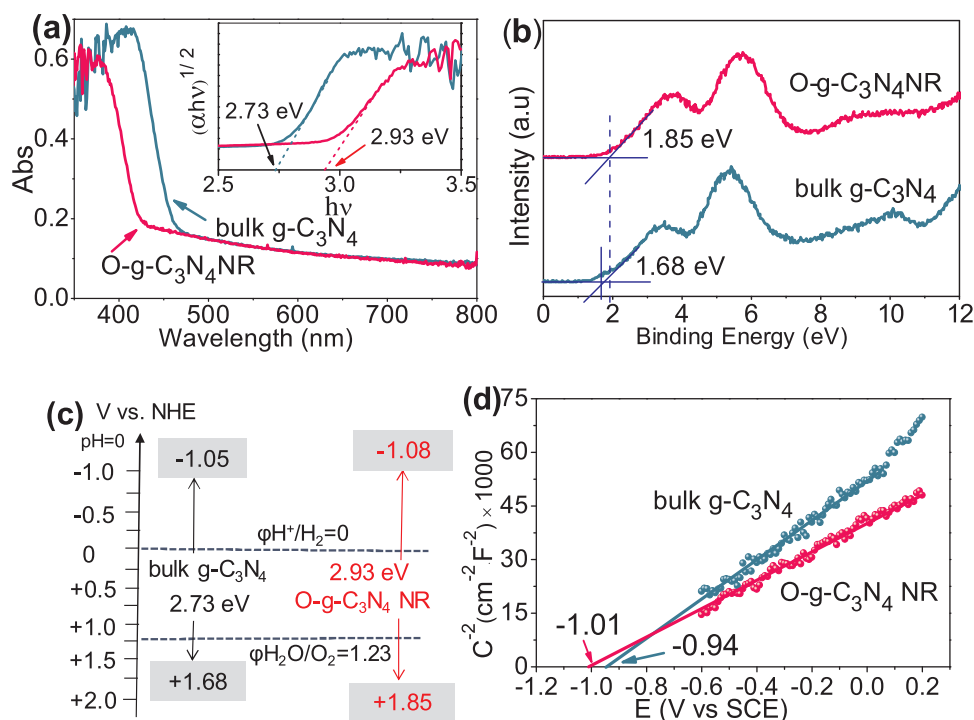


Fig. 4. (a) DRS spectra (inset is the corresponding Kubelka–Munk transformed reflectance spectra), (b) VB XPS spectra, (c) energy band structure of bulk g-C₃N₄ and O-g-C₃N₄ NR, and (d) Mott-Schottky plots at 10 kHz.

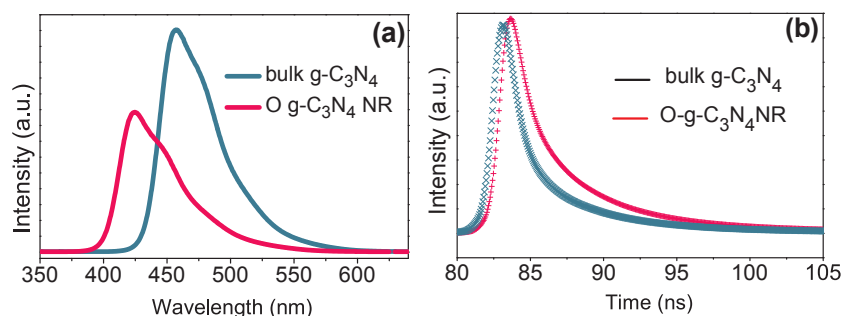


Fig. 5. (a) Fluorescence emission spectra and (b) time-resolved fluorescence excited by an incident light of 330 nm.

Table 1
Dynamics analysis of emission decays of bulk g-C₃N₄ and O-g-C₃N₄ NR.

Samples	A ₁ [%]	τ ₁ [ns]	A ₂ [%]	τ ₂ [ns]	A ₃ [%]	τ ₃ [ns]	τ _A [ns]
bulk g-C ₃ N ₄	40.47	0.81	47.19	4.59	12.33	28.26	1.65
g-C ₃ N ₄ NR	40.02	1.32	51.91	6.11	15.07	42.49	2.52

dehydration of bonding H₂O molecules in melamine fibers (Fig. S1b). After thermal polymerization, the melamine nanofibers were completely transformed into nanorods without the structures collapse (Fig. 1f). Furthermore, the nanorods were porous and defective characterizations (Fig. 1g) also testified by ESR spectra (Fig. S2a). An ESR signal with a *g* value of 2.003 is attributed to an unpaired electron on the carbon atoms of the aromatic rings within π -bonded nanorods. Compared to bulk g-C₃N₄, the much stronger spin intensity of the porous g-C₃N₄ nanorod (g-C₃N₄ NR) gave evidence for the promoted formation of unpaired electrons. In contrast, direct calcination of melamine powder produced bulk structure (Fig. 1b'–c'). The porous g-C₃N₄ NR showed a much larger specific surface area of 114.2 m²/g than 8.5 m²/g for the bulk C₃N₄ (Fig. S2b).

3.2. Calculations

Obviously, the formation of nanorods should be attributed to the nanofiber structure from the self-assembly of melamine units in

aqueous solution. The melamine units were linked together through strong hydrogen bonds among amino groups. The linked melamine units further formed fibers through Van der Waals force. The optimized structures from the density functional theory (DFT) calculation proved the proposed formation process of nanofibers (Scheme 1a and b). And the H₂O molecules were also inserted by hydrogen bonds. The DFT optimized structures of pristine g-C₃N₄ and O-g-C₃N₄ were shown in Scheme 1c and d. Their inter-planar distances are 6.85 and 8.054 Å, respectively.

DFT calculation was also applied to illustrate the optimized structure and the influence of oxygen on g-C₃N₄ which including band gap and h^+e^- separation. As shown in Fig. 2a, the calculated band gap of pristine g-C₃N₄ and O-g-C₃N₄ NR were 3.0 and 3.5 eV, respectively. The reason for the distinction between DFT and experimental value owing to monolayer model in our DFT calculation, that is, a bigger band gap for monolayer. The doped oxygen broadened the band gap, which was in agreement with the blue shift of absorption band edge aforementioned. Although the bandgap magnitude was overestimated, the trend in our calculations supported our interpretation of the DRS experiments. The wavefunction of the valence band is a combination of the HOMO levels of the g-C₃N₄ (Fig. 2b), which are derived from nitrogen *p_z* orbitals. The conduction band can similarly be connected to the LUMO of g-C₃N₄, predominantly consist of carbon *p_z* orbitals. While for O-g-C₃N₄ NR (Fig. 2c), owing to the oxygen linked of three melamine monomer and broke the symmetry of pristine g-C₃N₄, a more evident

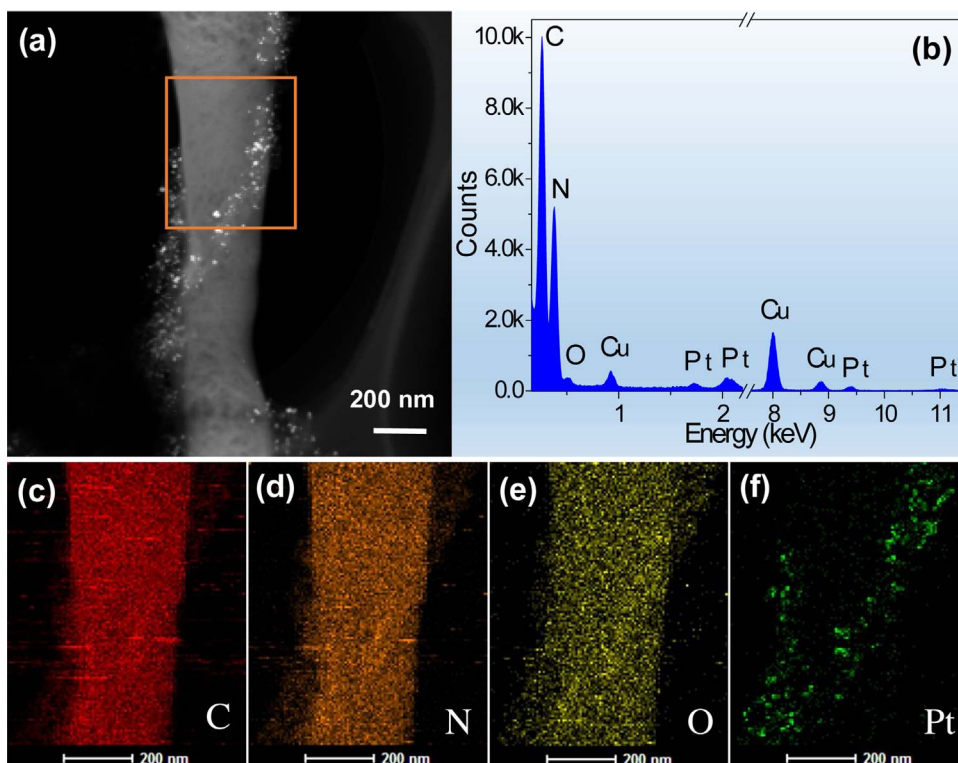


Fig. 6. (a) TEM image of 3 wt% Pt@O-g-C₃N₄ NR, (b) EDX spectrum from orange box in (a), and (c–f) elemental mappings of the selected orange area in (a). (For interpretation of the references to color in this figure legend, the reader is referred to the web version of this article.)

separation of electron/hole pairs were found. The contribution of LUMO is derived from the P_z orbitals of carbon which along with (100) direction and contribution of HOMO is derived from the P_z orbitals of nitrogen and oxygen in the plan of melem monomer. The calculations indicated that the inserted H₂O molecules was favourable for the formation of porous structure and the doped O was conducive to more efficient spatial charge separation between the electrons in the conduction band and the holes in the valence band.

3.3. Composition and photoelectrochemical properties

As shown in Fig. 3a, the Fourier transform infrared (FTIR) spectra for bulk g-C₃N₄ and O-g-C₃N₄ NR displayed the characteristic peak at 810 cm^{−1} for tri-s-triazine units and peaks at 1253, 1632 and 3200 cm^{−1} for nitrogen-containing groups [30,31]. Besides, O-g-C₃N₄ NR showed –OH groups at 2900–3300 cm^{−1} and C–O stretching vibration at 1205 cm^{−1}. The X-ray diffraction (XRD) patterns (Fig. 3b) showed that both bulk g-C₃N₄ and O-g-C₃N₄ NR had the (002) peak at 27.4° from interlayer stacking [32,33]. O-g-C₃N₄ NR had a larger interplanar distance (100) between nitride pores (10.5°, d = 8.319 Å) than bulk g-C₃N₄ (12.9°, d = 6.773 Å) [5–9], which was highly consistent with those in DFT optimized structures (Scheme 1). As indicated, the doped O atoms bridged adjacent tri-s-triazine units in O-g-C₃N₄.

The X-ray photoelectron spectroscopy (XPS) surveys demonstrated the C 1s, N 1s and O 1s peaks in both bulk g-C₃N₄ and O-g-C₃N₄ NR, especially a stronger O 1s peak in O-g-C₃N₄ NR than that in bulk g-C₃N₄ (Fig. 3c), corresponding to a stronger C–O bond peak in O-g-C₃N₄ NR (Fig. 3d). As shown in Fig. 3e, the high-resolution XPS spectra with Ar⁺ sputtering model revealed that the intensity of binding energy of O kept highly stable from 20 to 80 s, indicating that the homogeneous distribution of oxygen within the whole g-C₃N₄ nanorods, rather than on the surface. The N 1s peaks at 398.6, 399.3 and 401.0 eV arise from sp²-hybridized N in C–N=C, tertiary nitrogen N-(C)₃ and N–H bonds, respectively (Fig. 3f) [6–8]. The decreased N-(C)₃ peak in O-g-C₃N₄ NR should be attributed to the replacement of N-(C)₃ bonds with C–O bonds. In Fig. S3, the peaks at 285.0 and 288.3 eV are ascribed to sp²-hybridized C–C bonds in adventitious carbon species and sp²-

hybridized C (N–C=N) in aromatic skeleton rings, respectively [24–26]. The content of different atoms were listed in Table S1. The oxygen content increased from 2.38 mol% in bulk g-C₃N₄ to 9.91 mol% in O-g-C₃N₄ NR. The ratio of C–N=C/N-(C)₃ and C–N=C/N–H increased from 1.12 and 1.67 for bulk g-C₃N₄ to 1.41 and 3.21 for O-g-C₃N₄ NR, respectively, due to the replacement of sp³-hybridized N–C and C–N–H bonds with C–O bonds. The results further confirmed that doped oxygen bridged adjacent tri-s-triazine units in O-g-C₃N₄ NR.

Based on the results above, a possible mechanism of O-g-C₃N₄ NR formation was proposed in Scheme 2. When melamine was dissolved in water, melamine nanofibers were self-assembly formed through the strong hydrogen bond interactions and Van der Waals force. Thermal condensation transformed the supermolecular melamine units in the nanofibers into polymeric tri-s-triazine, obtaining O-g-C₃N₄ NR with an obviously decreased diameter. The H₂O molecules offered oxygen source for oxygen doping and played as porogen.

The optical properties were investigated by UV–vis diffuse reflectance spectra (DRS) (Fig. 4a). O-g-C₃N₄ NR showed a distinct blue shift of absorption edge compared with bulk g-C₃N₄. Their band gaps were calculated using Eq. (1):

$$\alpha = A(h\nu - E_g)^{n/2}/h\nu \quad (1)$$

where α is the absorption coefficient, A is a constant, h is the Planck's constant, E_g is the band energy, ν is the incident light frequency, and n is equal to 1 for the direct transition. The corresponding Kubelka-Munk transformed reflectance spectra were shown in the inset in Fig. 4a. The calculated bandgap energies were 2.93 and 2.73 eV for O-g-C₃N₄ NR and bulk g-C₃N₄. The blue shift should be attributed to O doping and quantum confinement effect [32]. The O doping into g-C₃N₄ altered valence band (VB) position from +1.68 for bulk g-C₃N₄ to +1.85 eV for O-g-C₃N₄ NR (Fig. 4b), due to the higher O 2p orbital energy than that of N 2p [34–36]. The DFT calculations also confirmed the VB shift. Obviously, more positive VB owns stronger potential for oxidation reactions to offer more electrons further for reduction reactions. The DRS results together with the VB-XPS analysis gave the conduction bands (CB) of O-g-C₃N₄ NR (−1.08 eV) and bulk g-C₃N₄ (−1.05 eV) (Fig. 4c),

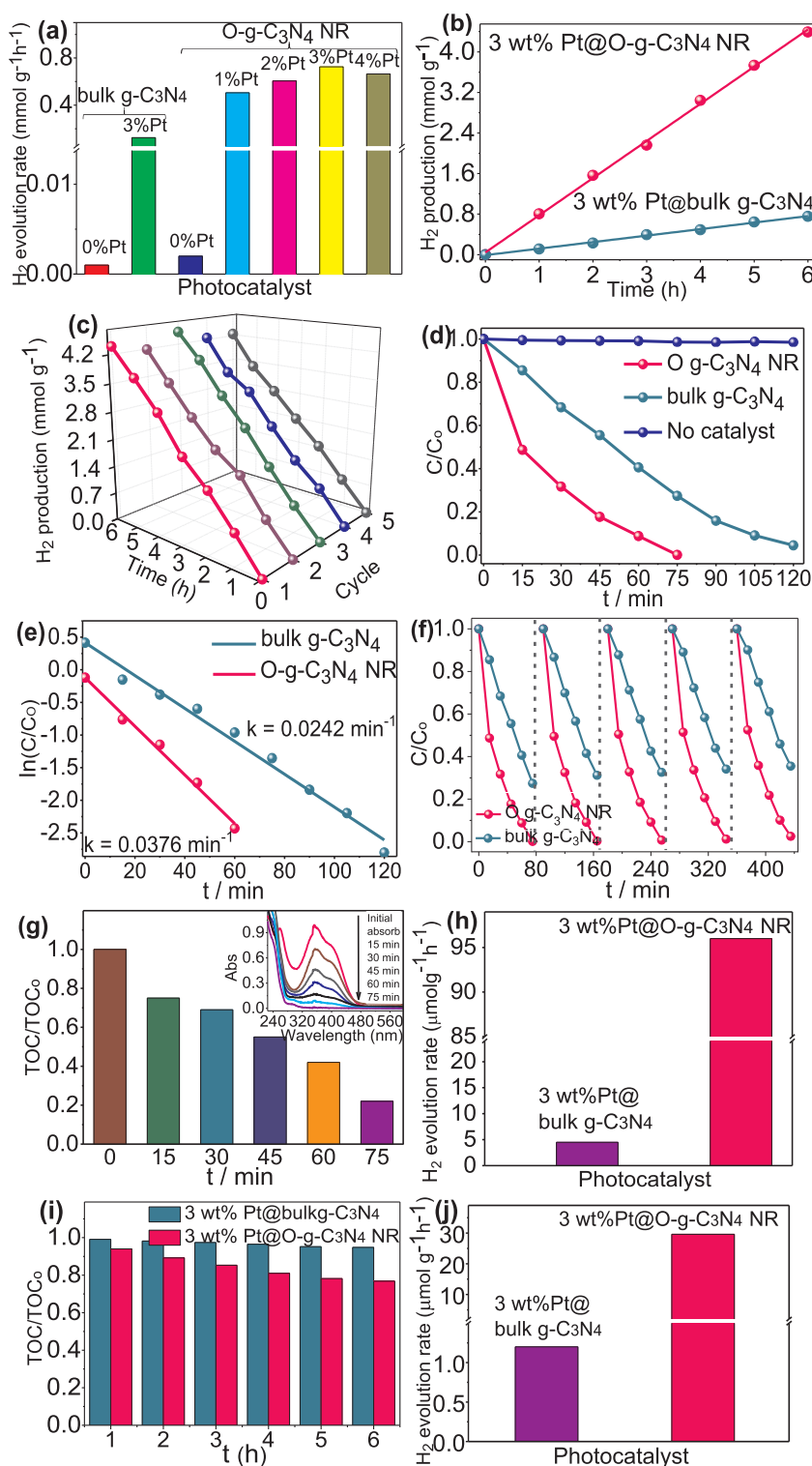
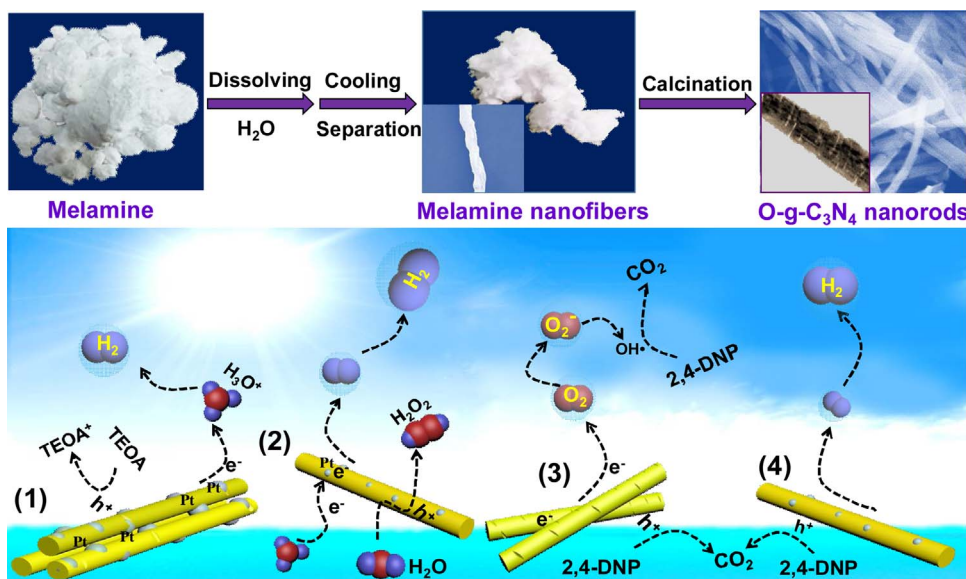


Fig. 7. (a) H₂ production over catalysts with different Pt loading, (b) H₂ production accumulation over catalysts, (c) cycling H₂ production over 3% Pt@O-g-C₃N₄ NR in 15 vol% TEOA, (d) 2,4-DNP degradation curves, (e) 2,4-DNP degradation kinetic curves, (f) photocatalytic stability in degrading 2,4-DNP, (g) TOC removal of 2,4-DNP degradation over O-g-C₃N₄ NR (the inset is UV-vis spectra of 2,4-DNP during photocatalytic degradation), (h) H₂ production, (i) TOC removal in 2,4-DNP degradation with H₂ evolution and (j) overall water splitting H₂ evolution.

well matching -1.01 and -0.94 eV from Mott-Schottky plots, respectively (Fig. 4d).

The photoluminescence spectrum could preliminarily evaluate the separation efficiency of photo-induced charge carriers in photocatalysts. The lower PL peak intensity of O-g-C₃N₄ NR than that of bulky g-C₃N₄ implied less photo-generated h^+ - e^- pairs recombination for O-g-C₃N₄ NR (Fig. 5a). Furthermore, the PL emission peak of O-g-CN NR blueshifted to ca. 425 nm from ca. 460 nm for bulk g-C₃N₄. The difference in PL emission wavelength are generally caused by the quantum confinement effect of nano-level materials, atomic defects and

impurity atom incorporations in catalyst [32–34]. Higher oxygen-doped content in g-C₃N₄ NR widened the bandgap together with the quantum size effect of nanorod, thus drove the blue shift to short wavelength region [35,36], which was also confirmed by DFT calculations (Fig. 2). The time-resolved photoluminescence (TRPL) spectra were applied to disclose the charge dynamic situation difference between bulk g-C₃N₄ and O-g-C₃N₄ NR (Fig. 5b). The TRPL decay spectrum curves were fitted by exponential decay kinetics function expressed as Eq. (2) [33,37–39]:



Scheme 3. Illustration of scalable production of porous oxygen-doped g-C₃N₄ NR and proposed photocatalysis charge transfer mechanism in (1) TEOA solution, (2) overall water splitting, (3) 2,4-DNP degradation under air and (4) simultaneous H₂ evolution and 2,4-DNP degradation for O-g-C₃N₄ NR under visible-light irradiation.

$$I(t) = A_1(\exp(-t/\tau_1)) + A_2(\exp(-t/\tau_2)) + A_3(\exp(-t/\tau_3)) \quad (2)$$

Meanwhile, the average emission lifetime (τ_A), reflecting the overall emission decay behavior, was calculated through Eq. (3):

$$\tau_A = (A_1\tau_1^2 + A_2\tau_2^2 + A_3\tau_3^2)/(A_1\tau_1 + A_2\tau_2 + A_3\tau_3) \quad (3)$$

where τ_1 , τ_2 and τ_3 are the emission lifetimes, and A_1 , A_2 and A_3 are the corresponding amplitudes. τ_1 is caused by the free excitons recombination in semiconductor while τ_2 and τ_3 are originated from the non-radiative recombination of charge carriers in the surface defect states. As listed in Table 1, the average emission lifetimes (τ_A) of bulk g-C₃N₄ and O-g-C₃N₄ NR were ~ 1.65 ns and 2.52 ns, respectively. It is believed that increased lifetime of photo-excited charges should be associated with promoted electron transport and modulated electronic structure by the quantum confinement effect and oxygen-contained electron acceptable groups [9–11].

In Fig. S4a, O-g-C₃N₄ NR exhibited a photocurrent density of $0.54 \mu\text{A cm}^{-2}$, two-fold higher than $0.24 \mu\text{A cm}^{-2}$ for bulk g-C₃N₄. Clearly, higher photocurrent means more separated electrons that would be subsequently migrated to catalysts' surface for redox reaction. As we well know, bulk g-C₃N₄ had a low electrical conductivity. O-g-C₃N₄ NR exhibited much smaller conductive resistance than bulk g-C₃N₄ (Fig. S4b), due to its 1D nanorod structure beneficial to photo-induced charge transfer and transport.

3.4. Photocatalytic performance

Platinum is the state-of-the-art hydrogen-evolution catalyst due to low overpotential and the optimal Gibbs free energy for proton [40,41]. Therefore, Pt nanoparticles were grown on the g-C₃N₄ NR by photo-deposition method. Ultrathin Pt nanoparticles were evenly distributed on the g-C₃N₄ NR, especially absorbed on the edges of nanorods because of rich active site exposure (Fig. 6a). The EDX spectrum disclosed the existence of C, N, O and Pt in the Pt@g-C₃N₄ NR composite (Fig. 6b). Elemental mapping displayed the homogeneous distribution of C, N, O and Pt atoms in the g-C₃N₄ NR (Fig. 6c–f).

Fig. 7a showed the H₂ production over the photocatalysts with different Pt loading (0, 1, 2, 3 and 4 wt%) in TEOA solution (80 mL, 15 vol%) under visible light ($\lambda > 420$ nm). Without cocatalyst Pt, O-g-C₃N₄ NR showed a H₂ production rate of $2 \mu\text{mol g}^{-1} \text{h}^{-1}$, two times higher than that of bulk g-C₃N₄. The rate increased up to maximum $732 \mu\text{mol g}^{-1} \text{h}^{-1}$ over 3% Pt@O-g-C₃N₄ NR, 5.7 times higher than $128 \mu\text{mol g}^{-1} \text{h}^{-1}$ over 3% Pt@bulk g-C₃N₄ (the optimized Pt loading

in bulk g-C₃N₄ was 3 wt%, Fig. S5a). With increasing irradiation time, H₂ production increased steadily (Fig. 7b). Furthermore, the H₂ production over O-g-C₃N₄ NR remained highly stable after five cycles (30 h) (Fig. 7c).

In the photocatalytic degradation process of 2,4-dinitrophenol (2,4-DNP) in air, the removal efficiency over O-g-C₃N₄ NR reached up to approximately 100% while that over bulk g-C₃N₄ was about 70% within 75 min (Fig. 7d). The degradation followed pseudo-first-order kinetic $\ln(C/C_0) = -kt$, where k is pseudo-first kinetic constant and t is time. The degradation rate over O-g-C₃N₄ NR ($k = 0.0376 \text{ min}^{-1}$) was about 1.55 times higher than that over bulk g-C₃N₄ ($k = 0.0242 \text{ min}^{-1}$) (Fig. 7e). It is well known that g-C₃N₄ itself owns the advantage of high stability and quick recovery without secondary pollution after water treatment. In the fifth run (each run for 75 min), the photocatalytic degradation efficiencies of 2,4-DNP still reached up to 98.1% and 67% over O-g-C₃N₄ NR and bulk g-C₃N₄, respectively (Fig. 7f), disclosing an excellent chemical stability and reliability for potential practical application. Accompanying with 2,4-DNP degradation over O-g-C₃N₄ NR (inset, Fig. 7g), the total organic carbon (TOC) removal efficiency achieved above 80% within 75 min (Fig. 7g). The active species trapping results indicated that the produced OH· radicals were the dominant oxidative species (Fig. S5b).

To evaluate the catalytic activity of simultaneous H₂ production with 2,4-DNP degradation, the photocatalytic reaction was carried out in N₂ atmosphere. The H₂ production rate over O-g-C₃N₄ NR reached $96 \mu\text{mol g}^{-1} \text{h}^{-1}$ far higher than $4.5 \mu\text{mol g}^{-1} \text{h}^{-1}$ over bulk g-C₃N₄ (Fig. 7h). After 6 h, the TOC removal of 2,4-DNP over O-g-C₃N₄ NR gradually decreased while that over bulk g-C₃N₄ varied little (Fig. 7i). Thus, it can be seen that the photo-generated electron-hole pairs in O-g-C₃N₄ NR were efficiently separated.

Excitedly, only in deionized water without using sacrifice agents, Pt/O-g-C₃N₄ NR displayed a considerable H₂ evolution rate of $29.6 \mu\text{mol g}^{-1} \text{h}^{-1}$, 24.7 times higher than $1.2 \mu\text{mol g}^{-1} \text{h}^{-1}$ over Pt/bulk g-C₃N₄ (Fig. 7j), accompanying with more H₂O₂ product (Fig. S5c and d). The apparent quantum yields (AQEs) of the photocatalytic hydrogen production over O-g-C₃N₄ NR reached 7.1%, 0.93%, and 0.29% at 420 nm in TEOA solution, 2,4-DNP solution, and deionized water, respectively (See experimental details in SI).

The remarkable photocatalytic performance of O-g-C₃N₄ NR should be attributed to the facts that (1) its high specific surface area and porosity provides large number of active sites and quick access to reactants, (2) the O dopant remarkably suppresses photo-induced h^+e^- pairs recombination and modulates electronic structure, and (3) energy

band configuration results in more powerful redox capacity.

The photocatalysis charge transfer mechanism in (1) TEOA solution, (2) overall water splitting, (3) 2,4-DNP degradation under air and (4) simultaneous H₂ evolution and 2,4-DNP degradation for O-g-C₃N₄ NR under vis-light irradiation was proposed in Scheme 3. Under irradiation, the electrons in the VB of g-C₃N₄ NR were excited to its CB, and then transferred to Pt for proton reduction. The generated holes in the VB (+1.85 eV) oxidized the sacrificial agent TEOA and converted H₂O molecules into H₂O₂. During 2,4-DNP degradation, the photogenerated electrons interacted with oxygen producing active species OH to oxidize 2,4-DNP into CO₂. In 2,4-DNP degradation with simultaneous H₂ evolution, hole oxidized 2,4-DNP to produce electrons for proton reduction to H₂.

4. Conclusion

In summary, well-defined g-C₃N₄ nanorods with porosity and oxygen doping were synthesized by directly heating hydrous melamine nanofibers. The obtained nanostructures exhibited outstanding photocatalytic activities towards overall water splitting and intractable organic pollutant degradation with simultaneous H₂ production under visible light. The proposed approach is featured by large-scale, low-cost, time-saving, environment-friendly and real-feasibility merits. It would be a universal strategy to develop element-doped g-C₃N₄ nanostructures by directly heating melamine precipitated from suitable solvents.

Acknowledgements

This work was supported by the National Natural Science Foundation of China (51778218 and 51478171), and Hunan Provincial Innovation Foundation for Postgraduate (CX2017B139 and CX2017B141).

Appendix A. Supplementary data

Supplementary data associated with this article can be found, in the online version, at <http://dx.doi.org/10.1016/j.apcatb.2017.10.042>.

References

- [1] J. Liu, Y. Liu, N. Liu, Y. Han, X. Zhang, H. Huang, Y. Lifshitz, S.-T. Lee, J. Zhong, Z. Kang, *Science* 347 (2015) 970–974.
- [2] J. Liu, J. Leng, K. Wu, J. Zhang, S. Jin, *J. Am. Chem. Soc.* 139 (2017) 1432–1435.
- [3] Y. Kang, Y. Yang, L.C. Yin, X. Kang, L. Wang, G. Liu, H.M. Cheng, *Adv. Mater.* 28 (2016) 6471–6477.
- [4] W.J. Ong, L.L. Tan, Y.H. Ng, S.T. Yong, S.P. Chai, *Chem. Rev.* 116 (2016) 7159–7329.
- [5] Q. Han, B. Wang, J. Gao, Z. Cheng, Y. Zhao, Z. Zhang, L. Qu, *ACS Nano* 10 (2016) 2745–2751.
- [6] Y. Zheng, L. Lin, X. Ye, F. Guo, X. Wang, *Angew. Chem. Int. Ed.* 53 (2014) 11926–11930.
- [7] Y. Zeng, C. Liu, L. Wang, S. Zhang, Y. Ding, Y. Xu, Y. Liu, S. Luo, *J. Mater. Chem. A* 4 (2016) 19003–19010.
- [8] D. Zheng, X.N. Cao, X. Wang, *Angew. Chem. Int. Ed.* 55 (2016) 11512–11516.
- [9] Z. Tong, D. Yang, Z. Li, Y. Nan, F. Ding, Y. Shen, Z. Jiang, *ACS Nano* 11 (2017) 1103–1112.
- [10] W. Xing, C. Li, Yu Wang, Z. Han, Y. Hu, D. Chen, Q. Meng, G. Chen, *Carbon* 115 (2017) 486–492.
- [11] W. Xing, C. Li, G. Chen, Z. Han, Y. Zhou, Y. Hu, Q. Meng, *Appl. Catal. B: Environ.* 203 (2017) 65–71.
- [12] B. Zhu, J. Zhang, C. Jiang, B. Cheng, J. Yu, *Appl. Catal. B: Environ.* 207 (2017) 27–34.
- [13] A. Li, X. Chang, Z. Huang, C. Li, Y. Wei, L. Zhang, T. Wang, J. Gong, *Angew. Chem. Int. Ed.* 55 (2016) 13734–13738.
- [14] V.W. Lau, I. Moudrakovski, T. Botari, S. Weinberger, M.B. Mesch, V. Duppel, J. Senker, V. Blum, B.V. Lotsch, *Nat. Commun.* 7 (2016) 12165.
- [15] X. Chen, Q. Liu, Q. Wu, P. Du, J. Zhu, S. Dai, S. Yang, *Adv. Funct. Mater.* 26 (2016) 1719–1728.
- [16] F. Dong, Z. Zhao, T. Xiong, Z. Ni, W. Zhang, Y. Sun, W.K. Ho, *ACS Appl. Mater. Interfaces* 5 (2013) 11392–11401.
- [17] Y. Kofuji, Y. Isobe, Y. Shiraishi, H. Sakamoto, S. Tanaka, S. Ichikawa, T. Hirai, *J. Am. Chem. Soc.* 138 (2016) 10019–10025.
- [18] Y. Ding, Y. Tang, L. Yang, Y. Zeng, J. Yuan, T. Liu, S. Zhang, C.B. Liu, S. Luo, *J. Mater. Chem. A* 4 (2016) 14307–14315.
- [19] M. Vázquez-González, W.C. Liao, R. Cazzelles, S. Wang, X. Yu, V. Gutkin, I. Willner, *ACS Nano* 11 (2017) 3247–3253.
- [20] Y. Zhao, F. Zhao, X. Wang, C. Xu, Z. Zhang, G. Shi, L. Qu, *Angew. Chem. Int. Ed.* 53 (2014) 13934–13939.
- [21] X. Yang, Z. Chen, J. Xu, H. Tang, K. Chen, Y. Jiang, *ACS Appl. Mater. Interfaces* 7 (2015) 15285–15293.
- [22] H. Yu, L. Shang, T. Bian, R. Shi, G.I. Waterhouse, Y. Zhao, C. Zhou, L.Z. Wu, C.H. Tung, T. Zhang, *Adv. Mater.* 29 (2017) 1605148.
- [23] H. Hou, F. Gao, L. Wang, M. Shang, Z. Yang, J. Zheng, W. Yang, *J. Mater. Chem. A* 4 (2016) 6276–6281.
- [24] Z. Chen, S. Pronkin, T.-P. Feller, K. Kailasa, G. Vilé, D. Albani, F. Krumeich, R. Leary, J. Barnard, J.M. Thomas, J. Pérez-Ramírez, M. Antonietti, D. Dontsova, *ACS Nano* 10 (2016) 3166–3175.
- [25] H.J. Li, D.J. Qian, M. Chen, *ACS Appl. Mater. Interfaces* 7 (2015) 25162–25170.
- [26] Y. Li, H. Xu, S. Ouyang, D. Lu, X. Wang, D. Wang, J. Ye, *J. Mater. Chem. A* 4 (2016) 2943–2950.
- [27] Q. Han, B. Wang, J. Guo, L. Qu, *Angew. Chem. Int. Ed.* 36 (2016) 11007–11011.
- [28] S. Guo, Z. Deng, M. Li, B. Jiang, C. Tian, Q. Pan, H. Fan, *Angew. Chem. Int. Ed.* 55 (2016) 1830–1834.
- [29] M.K. Bhunia, K. Yamauchi, K. Takanabe, *Angew. Chem. Int. Ed.* 41 (2014) 11181–11185.
- [30] Y. Shang, X. Chen, W. Liu, P. Tan, H. Chen, L. Wu, C. Ma, X. Xiong, J. Pan, *Appl. Catal. B: Environ.* 204 (2017) 78–88.
- [31] Y. Ding, Y. Tang, L. Yang, Y. Zeng, J. Yuan, T. Liu, S. Zhang, C. Liu, S. Luo, *J. Mater. Chem. A* 4 (2016) 14307–14315.
- [32] Z.F. Huang, J. Song, L. Pan, Z. Wang, X. Zhang, J.J. Zou, W. Mi, X. Zhang, L. Wang, *Nano Energy* 12 (2015) 646–656.
- [33] K. Zhang, L. Wang, X. Sheng, M. Ma, M.S. Jung, W. Kim, H. Lee, J.H. Park, *Adv. Energy Mater.* 6 (2016) 1502352.
- [34] R. Asahi, T. Morikawa, H. Irie, T. Ohwaki, *Chem. Rev.* 114 (2014) 9824–9852.
- [35] M.M. Khan, S.A. Ansari, D. Pradhan, M.O. Ansari, D.H. Han, J. Lee, M.H. Cho, *J. Mater. Chem. A* 2 (2014) 637–644.
- [36] M. Li, L. Zhang, M. Wu, Y. Du, X. Fan, M. Wang, L. Zhang, J. Shi, *Nano Energy* 19 (2016) 145–155.
- [37] W. Yang, L. Zhang, J. Xie, X. Zhang, Q. Liu, T. Yao, S. Wei, Q. Zhang, Y. Xie, *Angew. Chem. Int. Ed.* 55 (2016) 6716–6720.
- [38] M. Yan, Y. Hua, F. Zhu, L. Sun, W. Gu, W. Shi, *Appl. Catal. B: Environ.* 206 (2017) 531–537.
- [39] B. Lin, H. An, X. Yan, T. Zhang, J. Wei, G. Yang, *Appl. Catal. B: Environ.* 210 (2017) 173–183.
- [40] B. Jiang, Y. Sun, F. Liao, W. Shen, H. Lin, H. Wang, M. Shao, *J. Mater. Chem. A* 5 (2017) 1623–1628.
- [41] M. Zhu, Y. Osakada, S. Kim, M. Fujitsuka, T. Majima, *Appl. Catal. B: Environ.* 217 (2017) 285–292.